Article | Received 18 August 2026; Revised 28 September 2026; Accepted 23 October 2026; Published 17 November 2026
https://doi.org/10.55092/bm20260013

Stereolithography-fabricated β-TCP and HAp TPMS scaffolds: mechanical and biological performance of sheet and solid-based lattices

Tejas Koushik[1,†], Patrick McKendry[1,†], Catherine M. Miller[2] and Elsa Antunes[1,*]

[1] College of Science and Engineering, James Cook University, Townsville, Australia
[2] College of Medicine and Dentistry, James Cook University, Cairns, Australia

† These authors contributed equally to this work.

* Correspondence author; E-mail: elsa.antunes1@jcu.edu.au.

Highlights:

- β-TCP and HAp TPMS scaffolds produced using stereolithography.
- Comparison of sheet and solid based lattice topologies for bone repair.
- Solid-gyroid structures produced the highest compression strength.
- TPMS structures showed a limited effect on osteogenic differentiation.

Abstract: This study evaluates the mechanical and biological performance of Triply Periodic Minimal Surface (TPMS) scaffolds (gyroid and diamond) in two different lattice topologies (sheet and solid-based) using calcium phosphate-based materials. While natural trabecular bone exhibits a compressive strength of 20–80 MPa, current synthetic scaffolds often struggle to balance structural integrity with bioactivity. We investigated sheet and solid-based TPMS lattice topologies at porosities of 65% and 50%, manufactured using stereolithography of hydroxyapatite (HAp) and beta-tricalcium phosphate (β-TCP) slurries. Mechanical testing showed that solid-based lattice topologies provided superior performance, reaching compression strengths of up to 20 MPa, with solid-based gyroid geometries consistently outperforming diamond structures at porosities above 50%. On the other hand, sheet-based geometries offered compression strength less than 10 MPa across both HAp and TCP. Biologically, while both HAp and β-TCP supported cell proliferation and exhibited similar initial alkaline phosphatase (ALP) activity, HAp demonstrated higher structural strength at the cost of lower long-term bone mineralization. In contrast, β-TCP facilitated higher mineralization, suggesting a faster rate of biological integration. These findings indicate that while solid gyroid HAp scaffolds provide compression strength analogous to trabecular bone, the integration of β-TCP is essential for long-term osteoblast mineralisation. This research provides a framework for optimizing the trade-off between mechanical resilience and biological functionality in the design of next-generation BTE implants.

Keywords: additive manufacturing; TPMS scaffolds; calcium phosphate ceramics; bone tissue engineering

Copyright©2026 by the authors. Published by ELSP. This work is licensed under Creative Commons Attribution 4.0 International License, which permits unrestricted use, distribution, and reproduction in any medium provided the original work is properly cited.

1. Introduction

Bone tissues are self-healing when the defects are below a critical size; defects exceeding the critical size require scaffolds to support the healing process. Bone tissue engineering (BTE) techniques developed in the last decade have enabled healing of large bone defects, using scaffolds that mimic the mechanical support of natural bone tissue and the chemical cues to promote vascularisation. There are two main types of natural bone tissues; trabecular and cortical bone. Cortical bone forms the dense outer shell with a porosity less than 15%. Trabecular bone forms the inner lattice-like framework having porosities between 40%–90% to incorporate the bone marrow. This architecture enables load distribution near joints and long bones while also providing a high strength-to-weight ratio, and large surface area for mechanotransduction-driven remodelling. However, its load-bearing ability can vary depending on the location, loading direction and age of the individual. For example, the femoral head of the hip consists of both trabecular and cortical bone. Johannesdottir *et al.* [1] showed that during a sideways fall, cortical bone showed a higher contribution towards failure in older patients whereas, in younger patients the tissue level failure begins at the trabecular region. The trabecular region in long bones functions as a shock absorber whereas in vertebral bodies it functions as a primary load bearing structure [2]. Elastic modulus of trabecular bone depends on its density and typically ranges around 0.5 GPa. Furthermore, the structure retains its ability to bear load even after micro-fractures [3]. In this context, triply periodic minimal surface (TPMS) lattices are well suited for BTE because their smooth, interconnected pore networks reduce stress concentration while mimicking features of the natural trabecular bone [4].

TPMS structures such as primitive, gyroid and diamond are most explored for BTE applications [5,6]. For example, Kanwar *et al.* [7] showed that gyroid structures offered excellent strength and efficient load distribution while also facilitating osteointegration. Furthermore, they also show greater permeability and hence higher nutrition flux to support osteointegration. Split-P structures provide a similar performance, but also efficiently transfer mechanical stimulus to its surrounding tissues, consequently, preventing stress shielding [5,8]. Diamond structures show greater interconnectivity but offer higher stiffness compared to gyroid and primitive structures. This was reported as the primary reason for increased cell death in diamond structures [9], however, porous diamond-based Ti-6Al-4V scaffolds have showed bone regeneration ability in femur sites [10]. TPMS structures used in most of these studies are obtained using a solid unit cell. Sheet-based topologies on the other hand utilise a continuous wall to split the space into two separate structures. Due to the continuous wall, they offer a uniform stress distribution and are stiffer compared to network-based structures at equivalent porosities. Previous studies have shown that they can match the permeability and yield strengths of human trabecular bone [11]. However, there are limited studies that have explored and compared the use of sheet and solid-based TPMS lattices for bone tissue engineering.

While previously highlighted TPMS research predominantly focused on metallic alloys like Ti-6Al-4V, these materials lack the intrinsic mineralization capacity of calcium phosphate-based bioceramics. Direct ink writing and stereolithography of ceramics, such as hydroxyapatite (HAp) and beta-tricalcium phosphate (β-TCP), have opened new avenues for fabricating biomimetic TPMS lattices. Previous studies on calcium phosphate-based scaffolds featuring trabecular-like porosities (40%–75%) and pore sizes (100 μm–800 μm) have successfully demonstrated the stress-strain profiles and mature tissue integration required to mimic natural bone [5,12,13]. Furthermore, TPMS architectures mimicking

trabecular bone macroscopic properties (porosities of 55%–75% and pore sizes of 350 µm–700 µm) offer tunable compressive strength and angiogenic pathways to support vascularization [5,14]. The most preferred method of tuning scaffold properties involves adjusting porosity and wall thickness of the TPMS lattices or designing hybrid lattices [15,16]; this inevitably leads to compromises when designing for high strength or infiltration. Sheet-based structures are known to be highly permeable and have higher elastic moduli. Solid-based structures, while being less permeable, offer thicker walls to enable more efficient distribution of stresses [17,18]. Furthermore, since they are designed from the same TPMS structure, they can be smoothly blended to form a single hybrid lattice. To the best of my knowledge, there have been no studies using sheet and solid architectures to produce bioceramic BTE scaffolds. Hence, this study explores the performance of sheet- and solid-based configurations within gyroid and diamond TPMS geometries to mimic trabecular bone, utilizing the two most widely used bioactive ceramics: β-TCP and HAp. By systematically evaluating the structural performance of these sheet- *versus* solid-based topologies, this work aims to identify the optimal architectural strategy for bioceramic trabecular bone graft substitutes.

2. Methods

2.1. Scaffold design and 3D printing

In this study two lattice configurations, sheet-based and solid-based, were designed using two TPMS geometries: gyroid and diamond. Gyroid structures were chosen for their strong resemblance to natural bone tissue while diamond structures offered significant load bearing ability [19]. Sheet-based and solid-based TPMS structures were generated on nTopology and mapped onto a cylindrical volume with a diameter of 7 mm and height of 7 mm. Previous studies showed that structures with a porosity between 50%–70% by volume offer an ideal balance between mechanical and biological performance [20]. Furthermore, recommended pore sizes ranging between 200–800 µm have been known to be highly suitable for bone tissue engineering applications [21]. To ensure this pore size was achieved, target porosities of the structures were set at 65 vol% and 50vol% for sheet and solid network designs, respectively.

Lattice parameters available on nTopology include mid-surface offset and thickness, a description of these parameters are shown in our previous work [4]. Mid-surface offset measures the thickness of non-intersecting thin walls mainly seen in sheet-based structures. Lattice thickness selected for the unit cell represents the distance between consecutive non-intersecting surfaces. To ensure average pore sizes remained between 200–800 µm to enable cell seeding and attachment for *in vitro* analysis, lattice parameters were set according to Table 1. Designed structures were then converted to an STL file which was used as an input for the 3D printing process.

Table 1. Lattice parameters used to design scaffolds on nTopology.

Scaffold	Porosity	Unit Cell Size (mm)	Pore Size (µm)	Mid Surface Offset (mm)	Lattice Thickness
Sheet-Diamond	64%	1.7	650	0.35	0.5
Sheet-Gyroid	65%	1.3	600	0.35	0.5
Solid-Diamond	50%	1.8	640	-	-
Solid-Gyroid	50%	1.45	520	-	-

Scaffolds were 3D printed using stereolithography on a C100 EasyFab printer (3DCERAM, France), using HAp and TCP slurries with a layer height of 50 µm. Print settings and laser parameters were set using the manufacturer's guidelines. 3D printed parts were then cleaned using an airbrush to remove any uncured slurry before undergoing debinding. Debinded HAp and TCP parts were sintered at 1280 °C and 1100 °C (as shown in Figure 1), respectively, at a heating rate of 3 °C/min and a dwell of 60 min followed by cooling to room temperature at 3 °C/min.

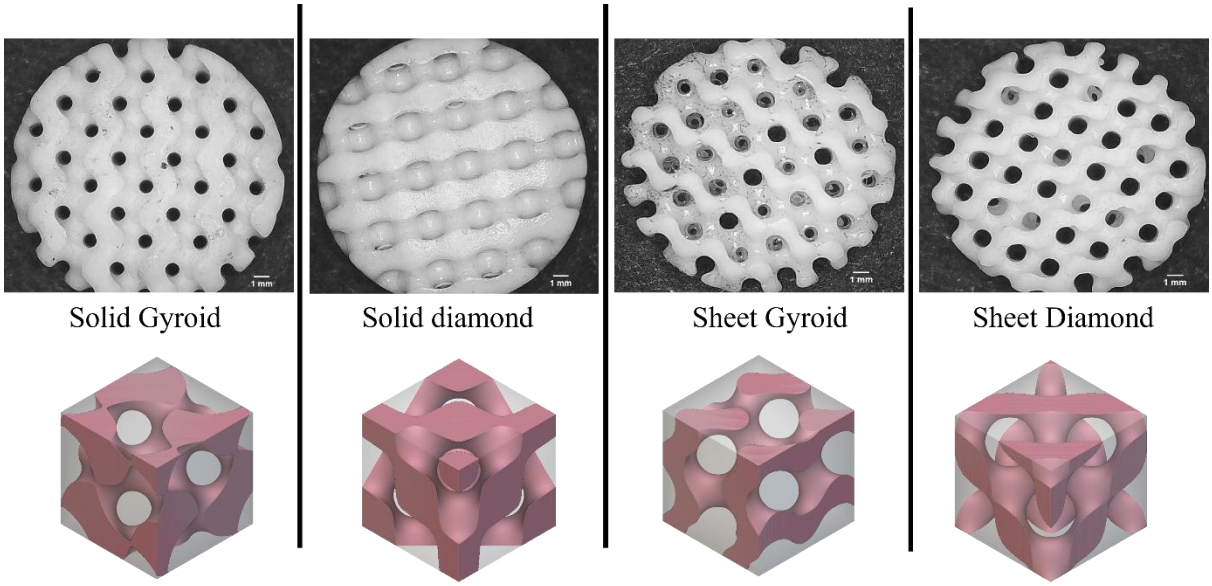


Figure 1. 3D-printed structures (top 4 images) along with their respective repeating unit cell (bottom 4 images).

2.2. Material characterization

Scanning electron microscopy (SEM, Hitachi SU5000) was used to characterise the surface morphology and grain sizes of HAp and TCP. Surfaces of the solid discs were prepared using a series of grinding papers (180, 320, 600, 800, 1200 and 2500) followed by polishing using a 1 µm diamond suspension and OP-S solution. The polished parts were then thermally etched at 100 °C below the sintering temperature used for each of the materials for 60 min. Crystalline phases of HAp and TCP were characterised using X-ray diffraction between 20 º–80 ºwith a step size of 0.02 ºand dwell time of 1 sec/step. Density of the sintered samples was measured using Archimedes principle, using the procedure outlined in ISO 18754.

2.3. Mechanical performance

Finite element method (FEM)—based homogenisation was used to determine the effective Young's modulus of the TPMS structures. Previous studies have shown the benefits of using this technique to predict the response of architected cellular solids [22,23]. An effective stiffness matrix is generated by conducting six independent static linear elastic simulations on the finite element mesh. Using these results a complete stiffness profile can be generated for any given architected solid [23,24]. This process was carried out using FEM tools available on nTopology (nTopology Inc,US).

Qualitative linear static analysis was completed using nTopology software, utilising integrated blocks to create mesh and boundary conditions. Analysis was completed by fixing the bottom face of each scaffold and applying a vertical load of 1 N to the opposite face. The material properties of HAP

and β-TCP were assigned to each geometry, as shown in the supplementary material (Table S1). The linear static analysis assumes that the load applied is sufficiently low, such that all local stresses are below the yield strength of the material and all strain is elastic. Stress values are, therefore, only indicative for each geometry and are used to compare stress profile of scaffolds and analyse data from experimental analysis.

Compression strength of the samples (7 mm diameter and 7 mm height) was measured at a displacement rate of 0.1 mm min^{-1} using the AUTOGRAPH AGS-X2 (Shimadzu, Japan). Tests were carried out in triplicates for each structure.

2.4. In-vitro analysis

In-vitro assays were performed to understand the influence of the gyroid and diamond structure on its ability to undergo osteointegration.

Human osteoblast cells (hOB; ATCC® CRL-3602) were cultivated in complete growth medium (CGM). The medium was comprised of Dulbecco's modified eagle medium (DMEM) supplemented with 10% fetal bovine serum, penicillin/streptomycin and L-glutamine. The cells were incubated in a 5% CO_2 incubator at 37 ℃ and 90% humidity and passaged when 95% confluence on the surface of the flask was reached. Passage number refers to the number of times a culture has been sub-cultured through harvesting and reseeding into daughter cell cultures [25]. Cells were used at passages 5 and 6. Reagents were sourced from Sigma Aldrich, Castle Hill, NSW, Australia.

For experiments, cells were detached from the surface of the tissue culture flask using 0.25% trypsin (Sigma-Aldrich, Castle Hill, NSW, Australia), an enzyme that aids in digesting proteins, and moved to a 15 mL test tube. A cell count was carried out on the solution, and the volume was adjusted with complete medium to create a cell concentration of 1×10^5 cells/mL. Sterile scaffolds were placed into the wells of a 24 well plate (Sigma Aldrich, Castle Hill, NSW, Australia). Triplicate samples of each scaffold type and material were used. 400 µL of medium containing cells was added to each well. Cells were allowed to attach to the surface of each scaffold overnight before cell medium was replaced to remove unattached cells.

Osteoblast proliferation was quantified using the AlamarBlue assay, which involves the conversion of resazurin to resorufin at days 1, 3, 7 and 10 to observe short- to medium-term cell proliferation in the samples [26]. A resazurin 10x stock solution was prepared by dissolving 0.5 g of resazurin salt in 100 mL of PBS. It was then added to each well to give a 1x concentration and the plate was incubated for 5 hours. A negative control of medium only was included on each plate. Following this, medium, in 100 µL triplicates, was transferred into a 96-well plate for absorbance measurement. Absorbance of resorufin was measured at wavelengths of 570 nm and 600 nm using a microplate absorbance reader (iMark Microplate Absorbance Reader, BioRad Laboratories, Hercules, CA, USA). A time-course analysis was then completed to evaluate and quantify baseline values for the metabolic activity of cells [27].

Alkaline phosphatase (ALP) activity of the hOB cells cultivated in a differentiation medium was measured using an ALP kit (ABCAM, Cambridge, United Kingdom). The ALP enzyme is crucial in the mineralisation of the extracellular matrix, promoting the release of inorganic phosphates and increasing the uptake of calcium [28,29]. Hence, quantifying the ALP activity of the cells will indicate the structure's ability to promote extracellular mineralisation during early stages. Structures were placed in a 24-well plate and seeded with hOB cells at a density of 7×10^4 and incubated for 7 days. On day 7,

cell medium was removed, and structures were washed with PBS before lysing cells in the lysis buffer provided. Cell lysates were collected and stored at −80 °C prior to measurement of absorbance using a microplate reader (FLUOStar Omega, BMG Labtech (Offenburg, Germany) at 405 nm. ALP activity of the cells (U/mL) was calculated against a calibration curve of p-nitrophenol standards. Analysis of each sample was performed in triplicate.

Alizarin red assay was performed to quantify the deposition of calcium in the cells. Structures were placed in a 24-well plate, seeded with hOB cells at a density of 1×10^6 and incubated for 21 days in growth medium supplemented with 10 mM β-glycerophosphate, 100 nM dexamethasone and 0.2 mM ascorbic acid (osteogenic medium). Medium was refreshed every 4 days. After 21 days, the medium was aspirated from the wells and cells on the structures were rinsed twice with PBS at room temperature. Cells were then fixed with 4% (v/v) PFA for 30 min, rinsed twice with PBS then 300 µL of 40 mM Alizarin red (Sigma-Aldrich, Castle Hill, NSW, Australia) in deionised water (adjusted to pH 4.2) was added to the cells and structures at room temperature. After incubating for 30 min, the Alizarin red was discarded, and the structures were placed in new wells. Structures were rinsed 5 times with deionised water and then incubated in PBS for 15-minutes at room temperature on a Grant ES-20 Compact Shaker-Incubator orbital rotator (150 rpm) (VWR International, Pty Ltd, Tingalpa, QLD, Australia). The PBS was then discarded, and cells were rinsed once with fresh PBS before being de-stained with 10% (w/v) cetylpyridinium chloride in 10 mM sodium phosphate (pH 7.0) for 15-minutes at room temperature on an orbital rotator (150 rpm). A 120 µL aliquot of extracted stain was then transferred to a 96-well clear plate to measure absorbance at 570 nm. Quantity of mineralisation as an amount of alizarin red (µM) was measured against a calibration curve of Alizarin red standards. Analysis of each sample was performed in triplicate.

2.5. Statistical analysis

Mean ± standard deviation was calculated for the data for the compression strength, proliferation assay, ALP assay and Alizarin red assay. The results were compared by Kruskal-Wallis and Mann Whitney tests. Multiple comparisons tests were carried out by Dunn's method using GraphPad Prism (GraphPad software, San Diego, CA). A $p < 0.05$ was considered to be statistically significant.

3. Results and discussion

3.1. Material characterisation

Measured solid density of the HAp sample was 94% ± 2%, with an average pore size of 1 µm and grain size of 1.16 µm (shown in Figure 2a). Sintered HAp showed a major peak at 31.8 °and some secondary peaks at 25.9 °, 32.2 °and 39.6 °(Figure 2b) which is typical for HAp. The peak at 31.8 °corresponds to hexagonally packed crystals, with unit cells comprising of calcium (Ca^{2+}), phosphate (PO_4^{2-}) and hydroxide (OH^-) ions where the hydroxide ions form the central support for the helical arrangements for phosphate ions [30,31].

β-TCP samples obtained a solid density of 97.5% ± 0.6% with pores approximately 0.1 µm and an average grain size of 3 µm (Figure 2c). While both α and β phases of TCP share a peak diffraction angle of 31 °, the β phase has secondary peaks as shown in Figure 2d at 27.9 °and 34.5 °, where α phase displays

very little diffraction intensity [32,33]. Hence the sintering cycles for HAp and β-TCP resulted in a grain size less than 3 μm with no phase changes but did not ensure full densification.

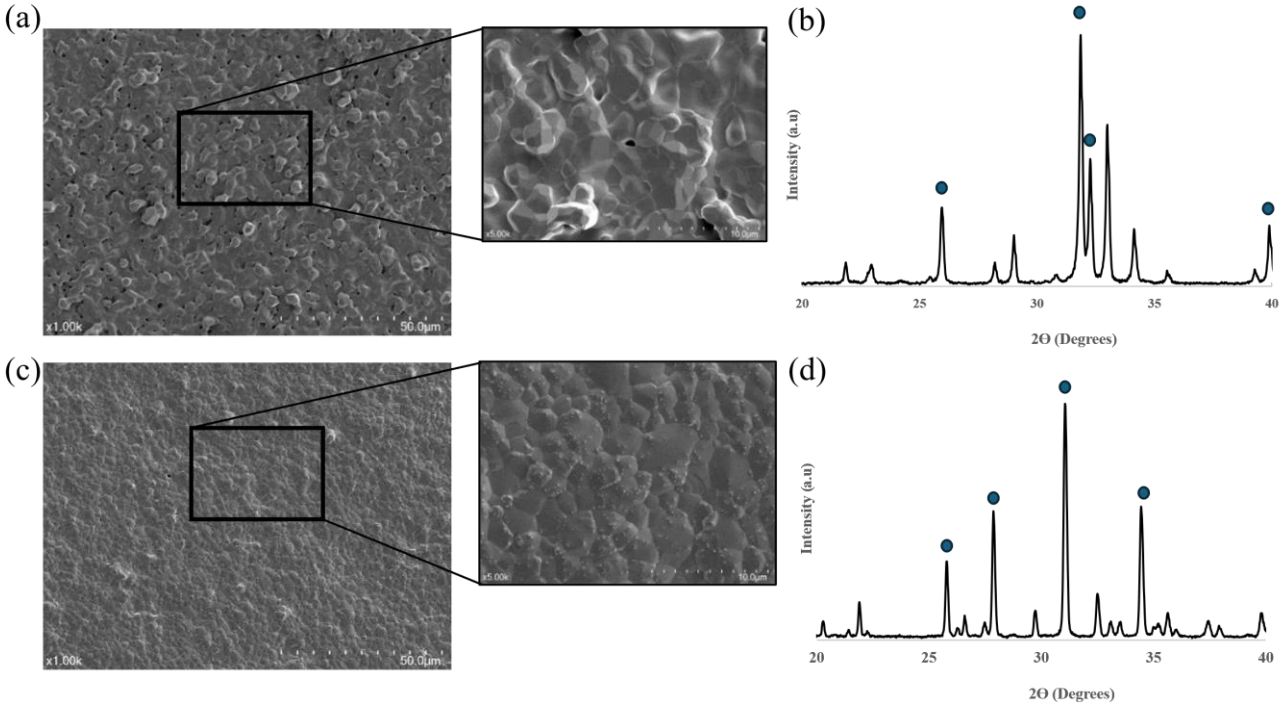


Figure 2. SEM and XRD results of sintered HAp and β-TCP. **(a)** Microstructure of the sintered Hap; **(b)** XRD data obtained from sintered HAp with major and minor peaks at 25.9 °, 31.8 °, 32.2 °and 39.6 °; **(c)** Microstructure of the sintered β-TCP; **(d)** XRD data obtained from sintered β-TCP with major and minor peaks at 25.7 °, 27.8 °, 31 °and 34.3 °.

3.2. Mechanical performance

3.2.1. Unit cell response

Homogenisation analysis was carried out in nTopology to visualise the stiffness of solid- and sheet-based gyroid and diamond TPMS unit cells. Gyroid unit cells showed an isotropic response whereas the diamond structures showed a relatively anisotropic response (as shown in Figure 3a). This difference in load-response is due to the inconsistent wall thickness in the diamond structures, hence there are more defects that will be produced in the positions with a smaller wall thickness of the structure during manufacturing [34].

The solid-diamond unit cell had the highest equivalent Young's modulus of 29.9 GPa, followed by the Solid-Gyroid unit cell with 27.0 GPa. The sheet network lattices had a maximum equivalent Young's modulus of 17.6 GPa and 14.7 GPa for the diamond and gyroid unit cells respectively. These differences in stiffness are due to the lower wall thickness of the sheet-based unit cells. The ratio of $\Delta E/E_{Max}$ was used to quantify the anisotropic index relative to the maximum stiffness. This is visualised in Figure 3b. indicating that solid network geometries are stiffer than their respective sheet network geometries, irrespective of unit cell type as shown in previous studies [35,36]. However, the response of the structure to load is more isotropic in the gyroid compared to the diamond unit cell in Figure 3a. Hence stiffness of an architected solid appears to be a function of the lattice configuration (sheet or solid) while the load response in different directions was a function of the lattice type.

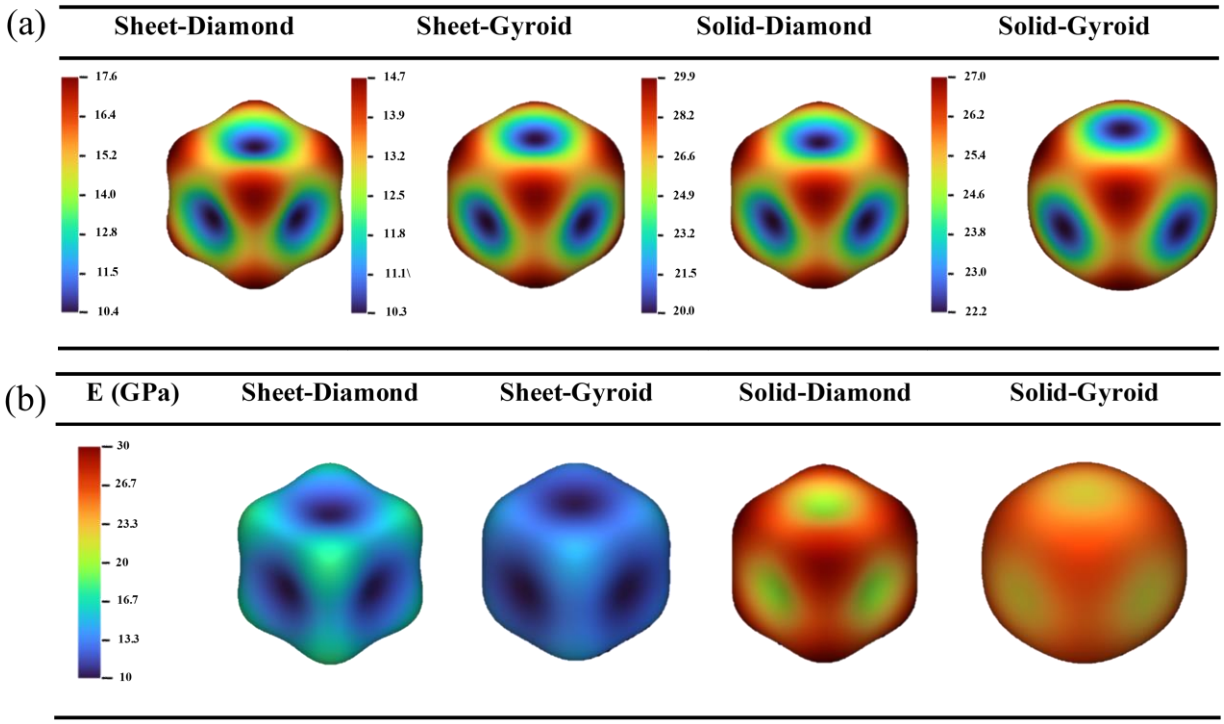


Figure 3. FEA analysis of diamond and gyroid lattices. **(a)** Stiffness of diamond and gyroid lattices with two network configurations (sheet and solid); **(b)** Young's modulus distribution measured in the gyroid and diamond structures.

3.2.2. Compression strength

Compression strength of the scaffolds was measured experimentally as shown in Figure 4a,b, where all the HAp structures showed an average compression strength almost twice that of β-TCP structures. HAp structures had an average compression strength ranging between 5–20 MPa whereas β-TCP structures showed a compression strength ranging 1.45–7.5 MPa despite having higher a sintered density.

The highest compression strengths were observed for the solid gyroid structures, reaching 7.55 ± 2.07 MPa and 20.36 ± 3.06 MPa for β-TCP and HAp, respectively. In contrast, the sheet diamond structures recorded the lowest values, at 1.45 ±0.17 MPa and 5.46 ±0.31 MPa for the β-TCP and HAp samples, respectively. The corresponding compression strengths of the solid diamond structure were 8.87 ± 1.08 and 5.28 ± 0.68 MPa in the β-TCP and HAp samples, while the sheet gyroid structures achieved 5.28 ± 0.68 MPa and 9.79 ± 0.62 MPa. All β-TCP and HAp structures show a quasi-brittle behaviour with the progressive damage to the TPMS structures. Localised failure of the structure during compression, indicated by an abrupt reduction in measured stress, protects the structure from the sudden catastrophic failure commonly observed in solid ceramic structures [37]. While there are no patterns that can be deduced from the stress-strain curves, sheet-based structures have a lower threshold to initiate failure when compared to their solid counterparts. The stress-strain curves of β-TCP structures shown in Figure 4c–f undergo localised failure starting at roughly 2 MPa with the exception of the solid gyroid structure. Similarly, HAp based structures shown in Figure 4g–j undergo localised failure starting at 2.5–3 MPa with the exception of the solid gyroid structure. Thin walls and a higher porosity of 65% observed in the sheet-based structures indicate the reasons for failure close to 2 MPa. The solid-diamond unit cell showed a peak stiffness of 29.9 GPa as mentioned previously, its anisotropic nature induced localised structural failures. These failures resulted

in discrete stress reduction rather than a singular catastrophic failure. In contrast, the solid-gyroid unit cell showed an isotropic response with only a few peaks observed on the stress-strain curve. Furthermore, the area under the stress-strain curves presented in the supplementary material (Figure S1) shows that both solid- and sheet-based gyroid structures provide greater toughness than their respective diamond structures.

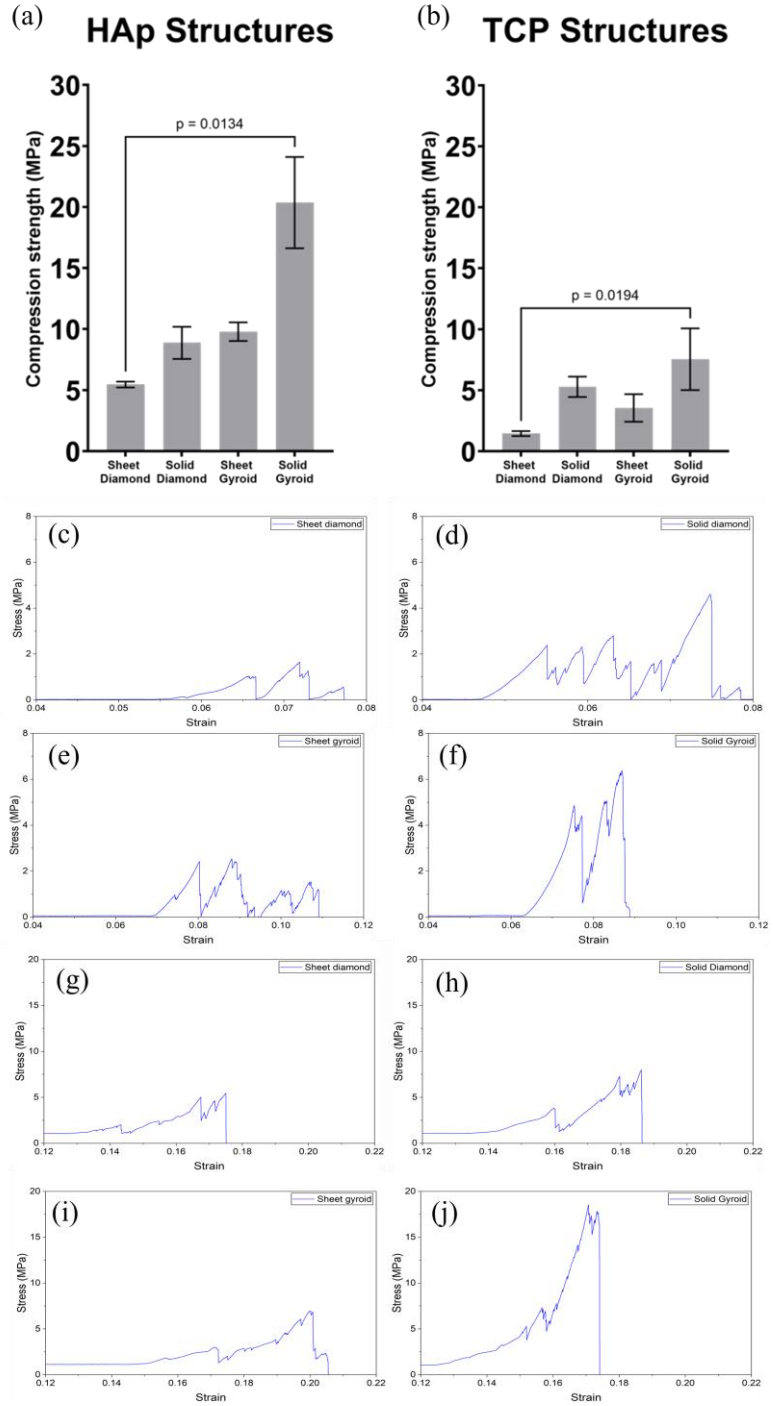


Figure 4. Compression strength and stress–strain response of HAp and β-TCP TPMS scaffolds. Average compression strength is shown for **(a)** HAp and **(b)** β-TCP scaffolds with sheet- and solid-based TPMS configurations. Data are presented as mean + standard deviation. Individual structures were compared using multiple comparisons tests using Dunn's method. Stress–strain curves are shown for β-TCP scaffolds: **(c)** Sheet-diamond; **(d)** Solid-diamond; **(e)** Sheet-gyroid and **(f)** solid-gyroid and for HAp scaffolds; **(g)** Sheet-diamond; **(h)** Solid-diamond; **(i)** Sheet-gyroid; **(j)** Solid-gyroid.

Finite element analysis of the applied compression on the scaffolds (Figure 5) show that sheet-based geometries generally exhibit high stress concentrations at the interior of their geometries compared to solid geometries (Figure 5). The stress response in the diamond architectures show vertically banded lines at the transition between unit cells whereas gyroid structures show a more diagonally distributed response. Previous studies have indicated that an X-shaped deformation mode is the most common failure mechanism observed in lattice-based structures [5,37,38]. This can be clearly observed from the broken fragments shown in the supplementary material (Figure S2). A similar deformation mode was also observed for the diamond structure. The configuration of the TPMS lattice, whether sheet or solid, did not have an impact on the failure mechanism.

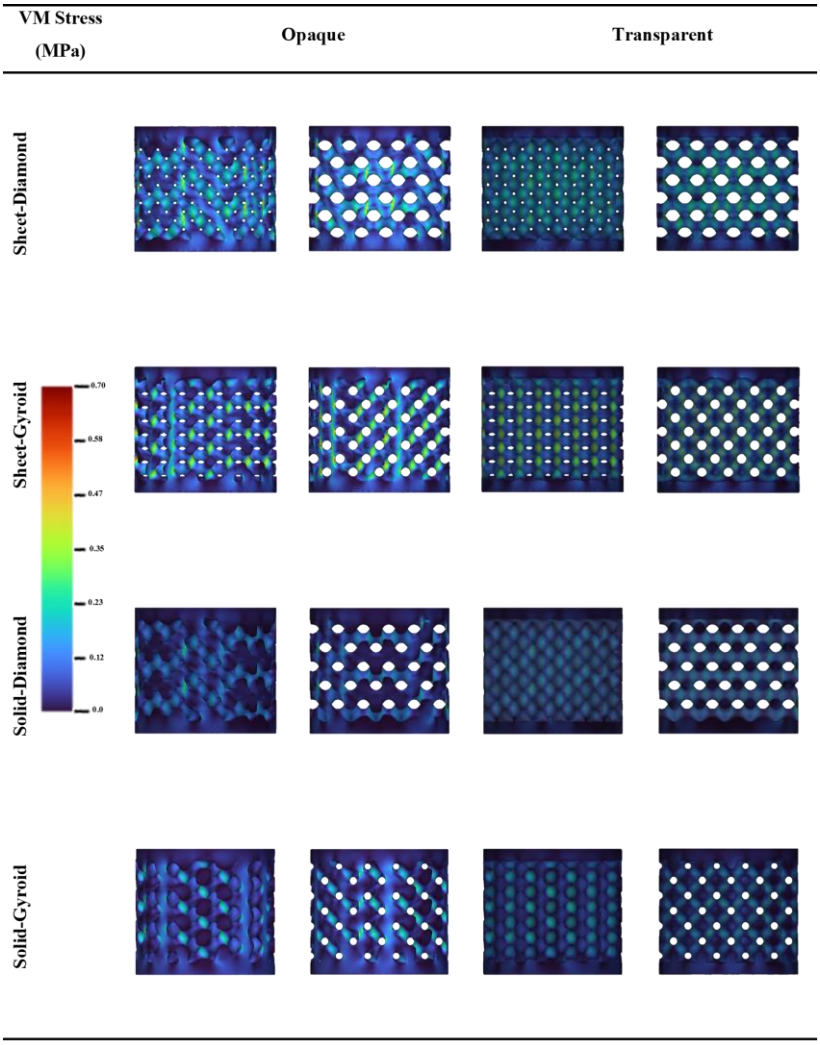


Figure 5. Qualitative linear static analysis of the gyroid and diamond structure in sheet and solid configurations. The transparent image shows the distribution of the stresses in the opposite viewing plane as that of the opaque image. Scale of the stresses range between 0–0.70 MPa which are well below the maximum compression strength of both HAp and TCP scaffolds in both sheet and solid configurations. The stress concentration seen is usually observed when the tessellating unit cannot fully repeat due to the geometric constraints of the cylindrical bounding box. This has, therefore, created beams on the outer boundary of all geometries with reduced sectional size causing a loss in local stiffness and strength. This leads to higher local compression strength in comparison to fully repeating units. Failure of all structures is expected to occur at each of these areas, as the stresses in these areas will reach the point of fracture or failure first.

On the other hand, gyroid structures showed a 168% increase in their compression strength when moving from a sheet to a solid network. On the contrary, diamond structures only demonstrated a 60% increase when moving from a sheet to a solid network. HAp structures showed a similar response but with a slightly higher threshold to initial failure (~2.5–3 MPa).

3.3. In-vitro characterisation

Cell proliferation was assessed in accordance with the methodology outlined previously. The percent reduction of resazurin to resorufin was calculated on days 1, 3, 7 and 10 for all the structures and materials and is shown in Figure 6. Osteoblast viability increased over the 10-day culture period, confirming cell attachment and proliferation on all scaffold groups. No significant differences in resazurin reduction were detected among scaffold architectures within either material group ($p > 0.05$; Figure 6a), or between β-TCP and HAp at any time point ($p > 0.05$; Figure 6b). Consistent with previous reports [39–41], stereolithography-fabricated β-TCP and HAp scaffolds exhibited no cytotoxic effects toward osteoblast cells.

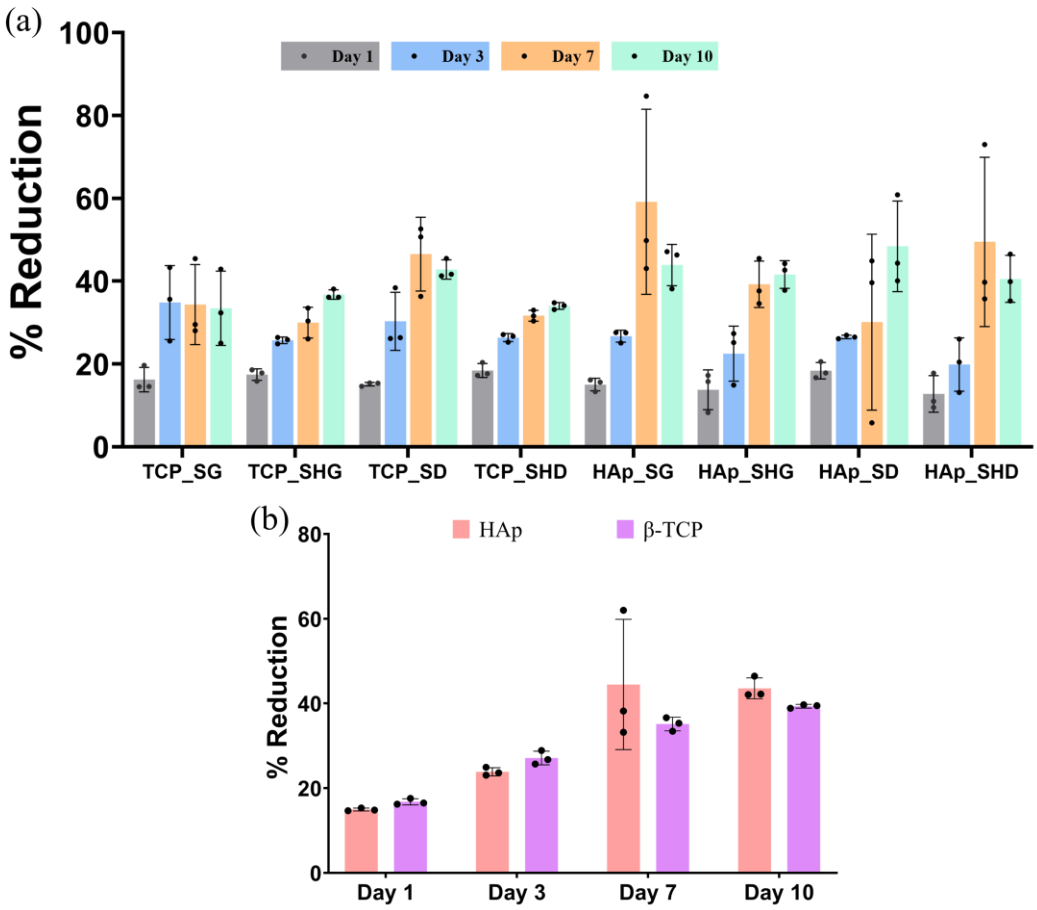


Figure 6. Proliferation assay results for TPMS structures. **(a)** Percentage reduction of resazurin observed in the cells seeded onto the β-TCP and HAp structures at intervals of 1, 3, 7 and 10 days. Results are plotted as mean ± SD of 3 samples. Each sample is abbreviated with the material type TCP or HAp followed by the structure; SG: Solid gyroid, SD: Solid diamond, SHG: sheet gyroid and SHD: sheet diamond; **(b)** Percentage reduction of resazurin observed on days 1, 3, 7 and 10 as function of material irrespective of structure. All results are presented as mean ± standard deviation of triplicate assays and results were compared using Mann Whitney tests. A $p < 0.05$ was considered to be statistically significant.

Synthesis and secretion of ALP by osteoblasts is a marker of early osteogenesis. Observed ALP activity of the structures is shown in Figure 7a, which shows no significant differences between the sheet or solid-based geometries and TCP and HAp materials. This is further confirmed by Figure 7b,c, where the mean values observed are nearly identical irrespective of structure type or material chemistry. Dos Santos *et al.* [42] showed that surface chemistry and topography of the TCP appeared to be more favourable for proliferation compared to HAp. Hence, reason for a similar response could be due to similar grain sizes achieved for HAp and β-TCP. Furthermore, 3D printing the scaffold layer-by-layer introduced similar surface roughness in both materials.

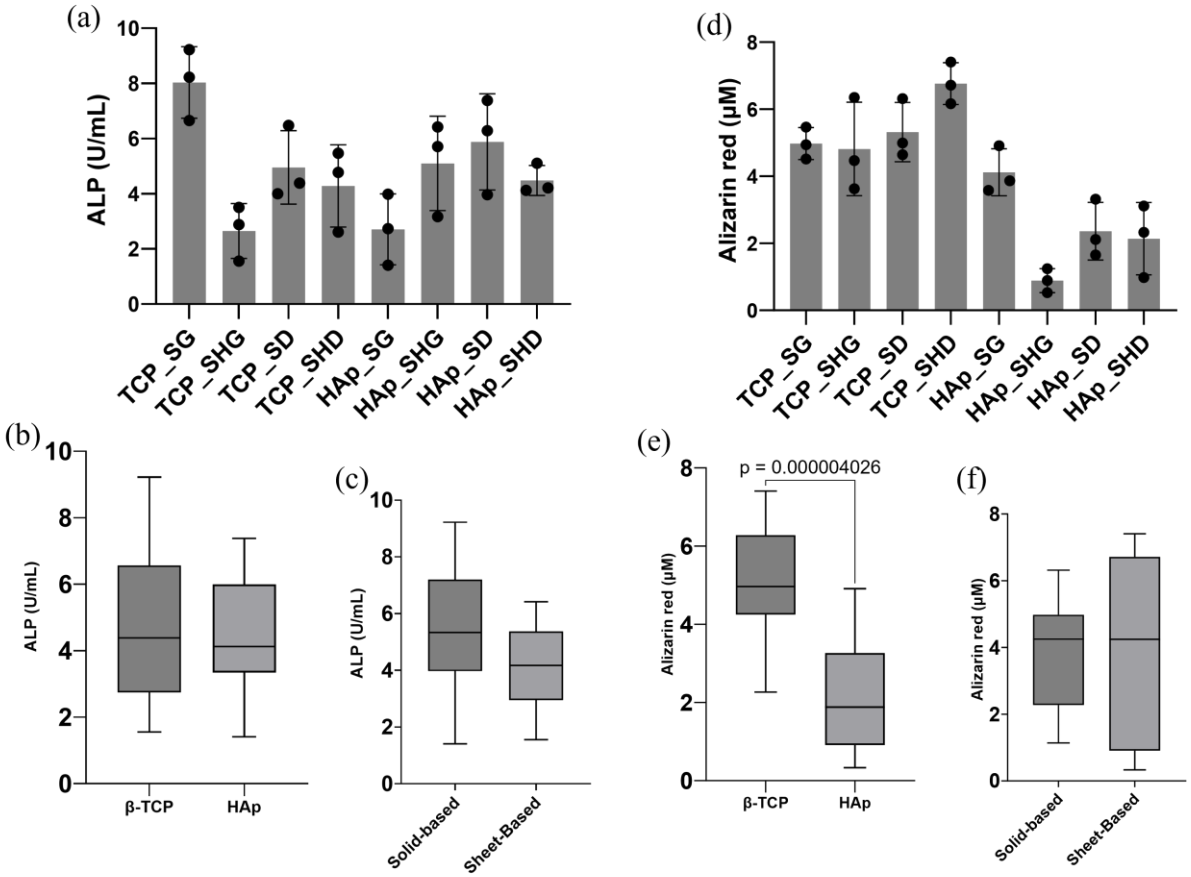


Figure 7. *In vitro* assay performance of TPMS structures. **(a)** Overview of the ALP activity observed for each scaffold group on day 7. Comparison of ALP activity as a function of **(b)** material composition and **(c)** lattice configuration (sheet *vs.* solid); **(d)** Overview of the mineralisation observed for each scaffold group on day 21. Comparison of mineralisation as a function of **(e)** material composition and **(f)** lattice configuration. All results are presented as mean ± standard deviation of triplicate assays and were compared using Kruskal-Wallis test followed by Mann-Whitney test to compare individual groups (sheet *vs.* solid and β-TCP *vs.* HAp). A $p < 0.05$ was considered to be statistically significant. SG: solid-gyroid, SD: solid-diamond, SHG: sheet-gyroid and SHD: sheet-diamond.

Alizarin red assay was used to quantify mineralisation after 21 days, as shown in Figure 7d–f. Lattice configuration and geometry had no significant effect on mineralisation (Figure 7f) under the tested conditions. In contrast, material chemistry had a significant effect, with β-TCP scaffolds showing higher mineralisation than HAp scaffolds ($p < 0.05$; Figure 7e). This response is likely associated with the faster dissolution of β-TCP, which promotes the release of calcium and phosphate ions into the surrounding

medium [43], resulting in supersaturation that can facilitate the precipitation of carbonate apatite on the scaffold surface [44]. By comparison, HAp is more stable, leading to a slower dissolution rate that can delay mineralisation. Hence, these findings are consistent with previous studies showing that the stronger ionic release from β-TCP contributes to enhanced mineralisation and greater osteoinductivity [40,42]. However, although these results align with findings in the literature, the absence of an acellular control makes it challenging to distinguish the effects of cellular activity from those of the material itself.

Overall, the results suggest that β-TCP enhances late-stage matrix mineralisation, whereas TPMS lattice type has a limited influence on osteogenic differentiation and mineral deposition under the tested conditions. Hence, future studies should investigate surface topographies of these 3D printed structures along with ion-release responses induced by the structure.

4. Conclusion

This study highlighted the comparative mechanical landscape between natural trabecular bone and TPMS lattice architectures. Trabecular bone exhibits a range of compression strength (1–20 MPa) and enables complex metabolic remodeling and stress distribution, TPMS structures can offer a tunable alternative while designing in-fill geometries for BTE implants. Furthermore, this study highlights the use of sheet and solid-based TPMS geometries to carefully tune the required mechanical behaviour.

Sheet-based lattices demonstrated a lower threshold for deflection and an anisotropic nature, with compression strength peaking at 10 MPa. In contrast, solid-based lattices proved more robust, offering compression strengths up to 20 MPa and a more versatile range of isotropic responses. Notably, the gyroid geometry emerged as the superior architecture at porosities exceeding 50 vol%, outperforming diamond structures. These findings suggest that while TPMS lattices, specifically solid gyroids, approximate the compression strength of human trabecular bone, further optimization of porosity and material composition is required to fully replicate the biomechanical resilience of natural bone.

While the structure dictates the mechanical environment, the choice of bioceramic material influences the biological outcome. This study confirms that while HAp and β-TCP both support biocompatibility, cell proliferation and mineral deposition, they fulfill distinct roles in bone tissue engineering.

HAp consistently demonstrated superior compressive strength regardless of TPMS geometry, making it a stronger candidate for load-bearing applications. However, this mechanical advantage was associated with lower mineralisation compared with β-TCP. Although both materials exhibited similar initial ALP activity, indicating comparable early-stage osteoblast differentiation, β-TCP was more effective in facilitating long-term mineral deposition. While *in vivo* studies are required to confirm these findings, the results suggest that a hybrid approach may be the most effective strategy. Balancing the structural rigidity of HAp with the enhanced bioactivity of β-TCP may be the most viable path for replicating the multi-functional nature of natural trabecular bone.

Data availability statement

Supplementary material accompanying this article includes Table S1, which describes the material properties applied during finite element analysis; Figure S1, which shows the area under the stress-strain curve measured for HAp and TCP structures; and Figure S2, which shows the diagonal and X-shaped shear bands observed after compression that corroborate the observations of the qualitative linear static analysis.

Declaration of generative AI and AI-assisted technologies

During the preparation of this manuscript, the authors used generative AI tools only to improve language and readability. Specifically, the authors used Co-pilot for language polishing only in limited sections of the manuscript. The authors take full responsibility for the content of the manuscript.

Authors' contribution

Conceptualization, T.K. and P.M; methodology, T.K. and C.M.M.; formal analysis, P.M.; investigation, P.M.; resources, C.M.M. and E.A.; writing—original draft preparation, T.K. and P.M.; writing—review and editing, C.M.M. and E.A.; visualization, T.K. and P.M.; funding acquisition, E.A. All authors have read and agreed to the published version of the manuscript.

Conflicts of interest

The authors declare no conflict of interest.

References

[1] Johannesdottir F, Thrall E, Muller J, Keaveny TM, Kopperdahl DL, *et al.* Comparison of non-invasive assessments of strength of the proximal femur. *Bone* 2017, 105:93–102.

[2] Oftadeh R, Perez-Viloria M, Villa-Camacho JC, Vaziri A, Nazarian A. Biomechanics and mechanobiology of trabecular bone: a review. *J. Biomech. Eng.* 2015, 137(1):010802.

[3] Osterhoff G, Morgan EF, Shefelbine SJ, Karim L, McNamara LM, *et al.* Bone mechanical properties and changes with osteoporosis. *Injury* 2016, 47:S11–S20.

[4] Koushik TM, Miller CM, Antunes E. Bone tissue engineering scaffolds: function of multi-material hierarchically structured scaffolds. *Adv. Healthcare Mater.* 2023, 12(9):2202766.

[5] Koushik TM, Miller CM, Antunes E. Graded hydroxyapatite triply periodic minimal surface structures for bone tissue engineering applications. *Adv. Healthcare Mater.* 2025, 14(25):2402953.

[6] Sun Y, Wang Y, Dong B, Yang P, Ji C, *et al.* Understanding the relationship between pore structure and properties of triply periodic minimal surface bone scaffolds. *J. Mater. Sci.: Mater. Med.* 2025, 36(1):6.

[7] Kanwar S, Al-Ketan O, Janarthanan G, Vijayavenkataraman S. Additively manufactured stochastic and gyroid scaffold design towards osseointegration and bone regeneration in a rabbit femur model. *Mater. Des.*2025, 250:113604.

[8] Verma R, Kumar J, Singh NK, Rai SK, Saxena KK, *et al.* Design and analysis of biomedical scaffolds using tpms-based porous structures inspired from additive manufacturing. *Coatings* 2022, 12(6):839.

[9] Castro APG, Santos J, Pires T, Fernandes PR. Micromechanical behavior of TPMS scaffolds for bone tissue engineering. *Macromol. Mater. Eng.* 2020, 305(12):2000487.

[10] Pei X, Wu L, Zhou C, Fan H, Gou M, *et al.* 3D printed titanium scaffolds with homogeneous diamond-like structures mimicking that of the osteocyte microenvironment and its bone regeneration study. *Biofabrication* 2021, 13(1):015008.

[11] Kelly CN, Lin AS, Leguineche KE, Shekhar S, Walsh WR, *et al.* Functional repair of critically sized femoral defects treated with bioinspired titanium gyroid-sheet scaffolds. *J. Mech. Behav. Biomed. Mater.* 2021, 116:104380.

[12] Fagotto-Clavijo R, Lodoso-Torrecilla I, Diez-Escudero A, Ginebra MP. Strategic advances in Vat photopolymerization for 3D printing of calcium phosphate-based bone scaffolds: a review. *Bioact. Mater.*2025, 52:719–752.

[13] Bouakaz I, Drouet C, Grossin D, Cobraiville E, Nolens G. Hydroxyapatite 3D-printed scaffolds with Gyroid-Triply periodic minimal surface (TPMS) porous structure: fabrication and an *in vivo* pilot study in sheep. *Acta Biomater.* 2023, 170:580–595.

[14] Chen WF, Wang BC, Liao GX, Tsai TY, Tseng YS. Physicochemical and biological evolution of biphasic TCP/CPP ceramics with DLP-printed TPMS geometries for bone tissue engineering. *Ceram. Int.* 2026, 52(20):36353–36367.

[15] Yang L, Li Y, Wu S, Chen P, Wu H, *et al.* Tailorable and predictable mechanical responses of additive manufactured TPMS lattices with graded structures. *Mater. Sci. Eng. A* 2022, 843:143109.

[16] Wang X, Yang H, Wang J, Guo X, Zhang L, *et al.* Design of zoned hybrid TPMS scaffolds for multi-performance optimization in bone tissue engineering. *Ceram. Int.* 2026, 52(17):32877–32888.

[17] Al-Ketan O, Lee DW, Rowshan R, Abu Al-Rub RK. Functionally graded and multi-morphology sheet TPMS lattices: Design, manufacturing, and mechanical properties. *J. Mech. Behav. Biomed. Mater.* 2020, 102:103520.

[18] Tang W, Zhou H, Zeng Y, Yan M, Jiang C, *et al.* Analysis on the convective heat transfer process and performance evaluation of Triply Periodic Minimal Surface (TPMS) based on diamond, gyroid and iwp. *Int. J. Heat Mass Transf.* 2023, 201:123642.

[19] Ma J, Li Y, Mi Y, Gong Q, Zhang P, *et al.* Novel 3D printed TPMS scaffolds: microstructure, characteristics and applications in bone regeneration. *J. Tissue Eng.* 2024, 15:20417314241263689.

[20] Torres-Sanchez C, Borgman JM, Sargeant B, Bell H, Alabort E, *et al.* Comparison of selective laser melted commercially pure titanium sheet-based triply periodic minimal surfaces and trabecular-like strut-based scaffolds for tissue engineering. *Adv. Eng. Mater.* 2022, 24(1):2100527.

[21] Dong Z, Zhao X. Application of TPMS structure in bone regeneration. *Eng. Regener.* 2021, 2:154–162.

[22] Mouman S, Koutsawa Y, Binsfeld L, Kirkayak L, Yang J, *et al.* Mechanical homogenisation of TPMS architectures: a comparison between finite element and mechanics of structure genome approaches. *Materials* 2025, 18(23):5357.

[23] Wang K, Cai M, Zhou P, Hu G. Homogenization in a simpler way: analysis and optimization of periodic unit cells with Cauchy–Born hypothesis. *Struct. Multidiscip. Optim.* 2021, 64(6):3911–3935.

[24] Friesecke G, Theil F. Validity and failure of the Cauchy-Born hypothesis in a two-dimensional mass-spring lattice. *J. Nonlinear Sci.* 2002, 12(5):445–478.

[25] Culture Collections. Cell line passage numbers explained. Available: https://www.culturecollections.org.uk/training-and-support/cell-line-passage-numbers-explained/ (accessed on 1 May 2026).

[26] García FI, García T, Torres LA, Ramírez V. Quantifying cell viability with resazurin assay. 2026. Available: https://tiarisbiosciences.com/wp-content/uploads/2026/08/TBK0505-0507.-Resazurin-Viability-Kit-Scientific-Application-Notes-v2.pdf (accessed on 1 May 2026).

[27] Duren Z, Chen X, Xin J, Wang Y, Wong WH. Time course regulatory analysis based on paired expression and chromatin accessibility data. *Genome Res.* 2020, 30(4):622–634.

[28] Piattelli A, Scarano A, Corigliano M, Piattelli M. Effects of alkaline phosphatase on bone healing around plasma-sprayed titanium implants: a pilot study in rabbits. *Biomaterials* 1996, 17(14):1443–1449.
[29] Rader BA. Alkaline phosphatase, an unconventional immune protein. *Front. immunol.* 2017, 8:897.
[30] Poralan GM, Gambe JE, Alcantara EM, Vequizo RM. X-ray diffraction and infrared spectroscopy analyses on the crystallinity of engineered biological hydroxyapatite for medical application. *IOP Conf. Ser.: Mater. Sci. Eng.* 2015, 79(1):012028.
[31] Muralithran G, Ramesh S. The effects of sintering temperature on the properties of hydroxyapatite. *Ceram. Int.* 2000, 26(2):221–230.
[32] Gallinetti S, Canal C, Ginebra MP. Development and characterization of biphasic hydroxyapatite/β-TCP cements. *J. Am. Ceram. Soc.* 2014, 97(4):1065–1073.
[33] Tavares D, de Oliveira Castro L, Soares G, Alves G, Granjeiro J. Synthesis and cytotoxicity evaluation of granular magnesium substituted Î²-tricalcium phosphate. *J. Appl. Oral Sci.* 2013, 21:37–42.
[34] Feng G, Li S, Xiao L, Song W. Mechanical properties and deformation behavior of functionally graded TPMS structures under static and dynamic loading. *Int. J. Impact Eng.* 2023, 176:104554.
[35] Jones A, Leary M, Bateman S, Easton M. Parametric design and evaluation of TPMS-like cellular solids. *Mater. Des.*2022, 221:110908.
[36] Maskery I, Ashcroft IA. The deformation and elastic anisotropy of a new gyroid-based honeycomb made by laser sintering. *Addit.Manuf.* 2020, 36:101548.
[37] Zhong M, Zhou W, Xi H, Liang Y, Wu Z. Double-level energy absorption of 3D printed TPMS cellular structures via wall thickness gradient design. *Materials* 2021, 14(21):6262.
[38] Lu C, Ding J, Jiang X, Wen P, Zhang C, *et al.* Enhancing mechanical properties and damage tolerance of additive manufactured ceramic TPMS lattices by hybrid design. *J. Am. Ceram. Soc.* 2024, 107(10):6524–6531.
[39] Li J, Li J, Yang Y, He X, Wei X, *et al.* Biocompatibility and osteointegration capability of β-TCP manufactured by stereolithography 3D printing: *in vitro* study. *Open Life Sci.* 2023, 18(1):20220530.
[40] Martinez JS, Peterson S, Hoel CA, Erno DJ, Murray T, *et al.* High resolution DLP stereolithography to fabricate biocompatible hydroxyapatite structures that support osteogenesis. *PLoS One* 2022, 17(8):e0272283.
[41] Le Guéhennec L, Van hede D, Plougonven E, Nolens G, Verlée B, *et al. In vitro* and *in vivo* biocompatibility of calcium-phosphate scaffolds three-dimensional printed by stereolithography for bone regeneration. *Journal of Biomedical Materials Research Part A* 2020, 108(3):412–425.
[42] dos Santos EA, Farina M, Soares GA, Anselme K. Chemical and topographical influence of hydroxyapatite and β-tricalcium phosphate surfaces on human osteoblastic cell behavior. *J. Biomed. Mater. Res. A* 2009, 89A(2):510–520.
[43] Baheiraei N, Nourani MR, Mortazavi SMJ, Movahedin M, Eyni H, *et al.* Development of a bioactive porous collagen/β-tricalcium phosphate bone graft assisting rapid vascularization for bone tissue engineering applications. *J. Biomed. Mater. Res. A* 2018, 106(1):73–85.
[44] Lu X, Leng Y. Theoretical analysis of calcium phosphate precipitation in simulated body fluid. *Biomaterials* 2005, 26(10):1097–1108.